

## Author Manuscript

**Title:** Diverse nanoassemblies of graphene quantum dots and their mineralogical counterparts

**Authors:** Nicholas Alexander Kotov, Dr.; Zhi-bei Qu; Wei-Jie Feng; Yichun Wang; Fedor Romanenko

This is the author manuscript accepted for publication and has undergone full peer review but has not been through the copyediting, typesetting, pagination and proofreading process, which may lead to differences between this version and the Version of Record.

**To be cited as:** 10.1002/anie.201908216

**Link to VoR:** <https://doi.org/10.1002/anie.201908216>

# Diverse nanoassemblies of graphene quantum dots and their mineralogical counterparts

Zhi-bei Qu<sup>1,2,3</sup>, Wei-Jie Feng<sup>1,2</sup>, Yichun Wang<sup>1,2</sup>, Fedor Romanenko<sup>4</sup>, Nicholas A. Kotov<sup>1,2,4,5\*</sup>,

<sup>1</sup>Department of Chemical Engineering, University of Michigan, Ann Arbor, MI 48109, USA;

<sup>2</sup>Biointerfaces Institute, University of Michigan, Ann Arbor, MI 48109, USA;

<sup>3</sup>School of Chemistry and Molecular Engineering, East China Normal University, Shanghai 200241, China;

<sup>4</sup>Department of Geomorphology and Paleogeography, Lomonosov Moscow State University, Leninskie Gory, Moscow 119991, Russian Federation;

<sup>5</sup>Department of Materials Science and Engineering, University of Michigan, Ann Arbor, MI 48109, USA;

\*E-mail: [kotov@umich.edu](mailto:kotov@umich.edu)

**ABSTRACT:** There is a growing understanding of the large role inorganic nanoparticles and their assemblies for Earth sciences. Complex structures from NPs are found in rocks, soils, and sea sediments but the mechanisms of their formation are poorly understood, which causes controversial conclusions about their genesis. Here we show that graphene quantum dots (GQDs), can assemble into complex structures driven by coordination interactions with metal ions commonly present in environment and serve a special role in Earth's history, such as  $\text{Fe}^{3+}$  and  $\text{Al}^{3+}$ . GQDs self-assemble into mesoscale chains, sheets, supraparticles, nanoshells, and nanostars. Specific assembly patterns are determined by the effective symmetry of the GQDs when forming the coordination assemblies with the metal ions. As such, maximization of the electronic delocalization of  $\pi$ -orbitals of GQDs with  $\text{Fe}^{3+}$  leads to GQD-Fe-GQD units with  $D_2$  symmetry, dipolar bonding potential, and linear assemblies. Variable dihedral angles in GQD-Al-GQD structural units destroys axial symmetric relationships and results in a more isotropic bonding potential with effective  $S_{2n}$  symmetry and, thus, the formation of supraparticles without preferred bonding axes. Taking advantage of high electron microscopy contrast of carbonaceous nanostructures in respect to ceramic background, the mineralogical counterparts of GQD assemblies are found in mineraloid shungite. The examined samples of shungite contain nanocarbons with nearly identical geometrical patterns, symmetry relations, and spectroscopic signatures as the laboratory superstructures, which may reflect self-assembly processes during its formation. These findings provide insight into nanoparticle dynamics during the rock formation that can lead to mineralized structures of unexpectedly high complexity.

**KEYWORDS:** self-assembly; symmetry; nanoparticles; graphene quantum dots, environment, electronic conjugation, nanoscale geology, nanoscale mineralogy.

**INTRODUCTION:** Self-assembly of different types of inorganic nanoparticles (NPs) is typically discussed in the context of engineering of advanced materials.<sup>1-6</sup> While the technological importance of NP superstructures and organized thin films is obvious, there is a growing acceptance of the important role that inorganic NPs play in geosciences,<sup>7,8</sup> climatology,<sup>9-12</sup> and even solar geoengineering<sup>13,14</sup>. In turn, this necessitates better understanding of their aggregation behavior that in most cases leads non-random agglomerates<sup>15</sup> with chemical and optical properties distinctly different from those of individual NPs.

The presence of NPs in different geological environments has been pointed out in several studies<sup>7,16-19</sup> but tracing their dynamic behavior in the same conditions is difficult due to limitations of electron microscopy and experimental models.<sup>20,21</sup> The connection between NP self-organization and geological and environmental processes was first identified by the studies of oriented attachment of nanocrystals<sup>22,23</sup> that may serve as example of non-classical crystallization<sup>24,25</sup> of many minerals. This is only example of many possible self-assembly processes involving nanocolloids,<sup>15,19-21</sup> especially when considering that there is a nearly infinite variety of nanoscale metal oxides, sulfides, silicates, and other particles present in Earth's water. As such, organized structures from NPs can be formed via coordination bonds that are known to produce numerous self-organized structures.<sup>26-30</sup> Since metal ions are abundant in the environment,<sup>31,32</sup> they can be, in fact, very common.

The first questions in this line of inquiry might be regarding the possible organization patterns and whether they are retained in minerals. Understanding the factors determining these patterns can shed light on ambient conditions and metal ions present at the time of rock formation. Among potentially many Earth science aspects, such knowledge can be instrumental for tracing the origin of mineralized formations with complex micro- and sub-micron geometries

known as microfossils.<sup>33</sup> These are found in many sedimentary and metamorphic rocks and take the shape of chains, shells, tubes, shells, and other organizational patterns (**Figure S1**). Because of their structural complexity and high content of carbon, these mineralized formations were attributed to the early life-forms,<sup>34</sup> which resulted in the ongoing scientific discussion about their genesis. If similar assembly patterns from NPs are possible, a simpler explanation of their appearance in mineralogical formations could be possible, as well.

## **RESULTS AND DISCUSSION:**

**Model Nanoparticles:** This study is focused on self-assembled structures of 2–10 nm segments of graphene sheets, also known as graphene quantum dots (GQDs).<sup>18,35–40</sup> Being quite different from oxide and chalcogenide nanocolloids whose self-assembly was previously studied,<sup>7,16,22,24,41–43</sup> GQDs represent a more accurate research model for the self-assembly processes that occur in Nature rather than other NPs because of the distinct chemical identities of carbonaceous NPs, which creates high electronic microscopy contrast on the background of ceramic matrices and enables spectroscopic traceability in laboratory and natural samples. The composition of individual NPs and their observed superstructures, for instance, for metal oxide NPs, can be altered dramatically in the course of mineralization. Furthermore, large amounts of anthropogenic nanocarbons makes understanding of their agglomeration processes paramount for understanding their fate in the environment. The fundamental questions that can be answered by GQD model system may also include the organizational patterns of carbonaceous NPs found in multiple minerals<sup>18</sup> as well meteorites<sup>44</sup> (**Figure S1b**).

**Morphology and Diversity:** GQDs were synthesized via an “oxidation-cutting” method<sup>45,46</sup> and were  $2.5 \pm 0.9$  nm in diameter and  $1.4 \pm 0.6$  nm in thickness as determined by transmission electron microscopy (TEM) and atomic force microscopy (AFM), respectively (**Figure S2**). They exhibit bright yellow-green fluorescence with a peak at 520 nm (**Figure S3**). The carboxyl edge-groups in GQDs made by oxidation cutting can form complexes with metal ions, and therefore, assembly of GQDs<sup>47</sup> via coordination bond bridges.

The ability of GQDs to self-assemble was investigated in the presence of various metal ions such as  $\text{Li}^+$ ,  $\text{Na}^+$ ,  $\text{K}^+$ ,  $\text{Ag}^+$ ,  $\text{Ca}^{2+}$ ,  $\text{Mg}^{2+}$ ,  $\text{Mn}^{2+}$ ,  $\text{Co}^{2+}$ ,  $\text{Ni}^{2+}$ ,  $\text{Cu}^{2+}$ ,  $\text{Zn}^{2+}$ ,  $\text{Cd}^{2+}$ ,  $\text{Pb}^{2+}$ ,  $\text{Al}^{3+}$ ,  $\text{Cr}^{3+}$ ,  $\text{Fe}^{3+}$ ,  $\text{Ce}^{3+}$ , and  $\text{Tb}^{3+}$  (**Figure 1**, **Figures S4-S8** in SI). A large variety of assembly motifs were observed. They may be categorized into two broad types: extended and terminal, exemplified by nanochains (**Figure 1d**) and supraparticles (**Figure 1b**), respectively.<sup>48</sup> Among the terminal assemblies, nanoshells (**Figure 1c**) and nanostars (**Figure 1f**) were also observed. For the extended assemblies, nanosheets were observed in some cases (**Figure 1e**).

To find a common parameter for the quantitative analysis of these dissimilar assembly patterns, we used the largest geometrical measure of GQD assemblies,  $I$ , (see legend in **Figure 1g**). Perhaps expectedly,  $I$  depends on the equilibrium binding constant,  $K_c$ , of metal ions to carboxyl groups (**Figure 1g**),  $K_c = [\text{R-COOM}^{n-1}] / [\text{M}^{+n}][\text{R-COO}^-]$ , which indicates that the energy of the coordination bonds represents the essential factor controlling the assembly. Metal ions can be divided into three groups with respect to their ability to induce GQD assembly. GQDs remain as single NPs in the presence of  $\text{Li}^+$ ,  $\text{Na}^+$ , and  $\text{K}^+$ , which are metals with a single positive charge and low  $K_c$ . Metal ions with double or triple positive charges and relatively low  $K_c$  such as  $\text{Ca}^{2+}$ ,  $\text{Mg}^{2+}$ ,  $\text{Mn}^{2+}$ ,  $\text{Co}^{2+}$ ,  $\text{Ni}^{2+}$ ,  $\text{Cd}^{2+}$ , and  $\text{Al}^{3+}$ , lead to supraparticles with sizes from 10 to 50 nm (**Figure 1b and S5**). The supraparticles assembled with  $\text{Al}^{3+}$  ions showed a spherical

morphology with a diameter of  $43 \pm 6$  nm. The size uniformity index,  $S$ , (see Figure S2 in SI) of the supraparticles was calculated to be 13.8%. Similarly to the previous observations of supraparticles self-assembled from nanoscale units,<sup>49</sup> we observed a substantial decrease of  $S$  for assembled terminal structures. Size uniformity for pristine GQDs were 33.7% for diameter and 46.1% for thickness, respectively (**Figure S2**).

Highly charged metal ions with high  $K_c$  such as  $\text{Fe}^{3+}$ ,  $\text{Cu}^{2+}$ ,  $\text{Zn}^{2+}$ ,  $\text{Pb}^{2+}$ ,  $\text{Cr}^{3+}$ ,  $\text{Ce}^{3+}$ , and  $\text{Tb}^{3+}$ , lead to the assembly of GQDs into nanochains (**Figure S7**). GQD assemblies for  $\text{Ni}^{2+}$  ions form nanoshells (**Figure 1c**) with a diameter of 60–200 nm and a wall thickness of  $18 \pm 8$  nm. Note that such classification of ions with respect to the types of assemblies formed is empirical and can be expanded once other types of geometries in the superstructures are observed. Modification of the GQDs with other anionic functionalities beyond carboxyl groups will further expand the spectrum of self-assembled structures.

**Nanoscale Structure:** Considering the special role of iron ions in Earth's mineralogy and evolution<sup>50,51</sup> as well as its highest abundance among transition metals on Earth,<sup>31</sup> we chose to investigate the assemblies of GQDs with  $\text{Fe}^{3+}$  in greater detail. Among all the metal ions tested,  $\text{Fe}^{3+}$  ions produced assemblies with the largest  $\Gamma$ . The GQD- $\text{Fe}^{3+}$  nanochains will serve as the primary model for the following experimental series aimed at better understanding of the structural features and formation mechanisms of GQD coordination assemblies.

Detailed studies of the effects of solvents, concentrations, pH, and other parameters (Figure S8-S14 in SI) showed that the propensity of GQDs to assemble was the highest when in water at pH 3.2 with  $[\text{Fe}^{3+}] = 0.5$  mM and  $[\text{GQD}] = 10$   $\mu\text{g/mL}$ . The GQD- $\text{Fe}^{3+}$  nanochains were as long as  $2400 \pm 900$  nm (**Figure S12**) and had an aspect ratio  $\Gamma/D > 160$ , where  $D$  is the average

diameter/width of the nanochains. Neither different solvents nor GQD concentration between 1  $\mu\text{g/mL}$  and 100  $\mu\text{g/mL}$  exhibited a strong effect on the morphology of the assemblies or  $L$  indicating that these parameters are primarily determined by the strength of coordination bonds between  $-\text{COO}^-$  and  $\text{Fe}^{3+}$  and not by hydrophobic forces. The strong dependence of  $D$  on the dielectric constant,  $\epsilon$  (**Figure S9**), indicates that electrostatic GQD-GQD repulsion plays a key role in the formation of nanochains.

Scanning transmission electron microscopy (STEM) showed that the GQD- $\text{Fe}^{3+}$  nanochains have a fractal geometry (**Figure 2**) with fractal dimension of 1.3, indicating that they can be largely described as a one dimensional object. The width of the nanochain,  $D$ , was an average of  $7.4 \pm 2.7$  nm along the entire assembly, which is quite remarkable for a spontaneously formed structure from components with low size uniformity, indicating thermodynamic control of this assembly parameter. Simultaneously, the length of the assemblies  $L$  ranged from 500 nm to 3000 nm; such variability is characteristic of kinetic control of the chain elongation. From high resolution high angle annular dark field (HAADF) STEM images, single GQDs can be recognized along the nanochains; their size was 2–4 nm, which is consistent with that for unassembled GQDs (**Figure 2c**). The constitutive units showed lattice spacing of 0.25 nm (**Figure 2d**), which corresponds to (1120) lattice fringes of graphene. TEM tomography (**Figure 2e** and video in SI) indicate that GQD- $\text{Fe}^{3+}$  nanochains are homogeneous with no obvious differences found between their inner and outer parts of the nanochains (**Figure S15** in SI). The height,  $H$ , of the nanochains obtained from AFM (**Figure 2f**) was  $4.6 \pm 1.9$  nm, which is comparable to the values of  $D$  obtained from STEM (**Figure 2c**).

**Mechanism of Assembly:** Elemental analysis by XPS showed that the GQD- $\text{Fe}^{3+}$  nanochains consist of carbon, oxygen, nitrogen, and iron, with an atomic ratio as 62.5 : 36.0 : 1.0 : 0.5,

which largely matched the elemental analysis obtained by energy dispersive analytical spectroscopy (EDAX) (**Figure S16**). Nitrogen comes from the doping nitrogen at GQDs when nitric acid was added for the oxidative cutting during the synthesis process.

The strong fluorescence of GQDs makes it possible to observe the formation of nanochains in situ using confocal fluorescence microscopy. The dispersion of GQDs without  $\text{Fe}^{3+}$  showed randomly distributed fluorescent dots (**Figure S17** in SI). After addition of 0.5 mM  $\text{Fe}^{3+}$ , GQDs quickly assembled into chains; the luminescence maximum was enhanced and shifted from 520 nm to 550 nm (**Figure S3**). After three minutes, brightly fluorescent GQD- $\text{Fe}^{3+}$  nanochains were observed. Their length was between 1  $\mu\text{m}$  and 20  $\mu\text{m}$ , which coincides with  $l$  obtained from TEM data.

The formation of COO-Fe coordination bonds were detected by Fourier transform infrared spectroscopy (FT-IR, **Figure 3a**). Dispersed pristine GQDs showed a peak at 1695  $\text{cm}^{-1}$ , corresponding to the stretching vibration in  $-\text{COOH}$  groups. For the GQD- $\text{Fe}^{3+}$  nanochains, the IR peak split into the symmetric 1653 and asymmetric 1406  $\text{cm}^{-1}$  of the ionized carboxyl groups  $-\text{COO}^-$ . Confirming the FT-IR data, high resolution XPS spectra (**Figure 3b, c** and **S18** in SI) before and after the formation of GQD- $\text{Fe}^{3+}$  nanochains, demonstrated strong charge transfer from  $-\text{COO}^-$  to  $\text{Fe}^{3+}$  (**Supplementary Notes**) and the formation of the coordination bonds. UV-Vis absorption and magnetic circular dichroism (MCD) spectroscopies confirm this conclusion (**Figure S19**). From the cumulative analysis of all these experimental series, the formation of  $-\text{COO}^- \text{--} \text{Fe}^{3+}$  coordination bonds is readily inferred (**Supplementary Notes**). The experimental dependences of geometrical parameters of GQD assemblies on the media, pH, ions and their concentrations (**Figure S2-S8**), are consistent with the self-assembly process being governed by



the counterbalance of attractive forces from coordination interactions and repulsive forces from electrostatic interactions of GQDs.

The Raman spectra can provide information about both the carbonaceous assemblies prepared in the laboratory and those formed in Nature. Unassembled GQDs showed a *D* band at 1378  $\text{cm}^{-1}$ , a *G* band at 1602  $\text{cm}^{-1}$ , and a weak and broad *G'* band around 2713  $\text{cm}^{-1}$  (**Figure 3d**). Interestingly, GQD- $\text{Fe}^{3+}$  nanochains showed 4.8 times stronger Raman signals at 1370  $\text{cm}^{-1}$  and 1592  $\text{cm}^{-1}$  for the *D* and *G* bands respectively, compared to those from free GQDs. The *G'* bands for GQD- $\text{Fe}^{3+}$  nanochains showed a multicomponent shape with two maxima at 2726 and 2896  $\text{cm}^{-1}$ . The split in *G'* band corresponds to GQD stacking in the assemblies.<sup>52</sup>

The electronic structure of the coordination assemblies of GQDs elucidated by density functional theory (DFT) points to the origin of the linear motif in GQD assemblies. After energy optimization, the structure of GQD- $\text{Fe}^{3+}$  dimers showed a dihedral angle of 73.3 degrees from one GQD plane to the other. The HOMO and LUMO for GQD-GQD- $\text{Fe}^{3+}$  assemblies (**Figure 4c and 4d**) displayed remarkable long-range conjugation between the aromatic systems of GQDs despite their twisted orientation and large value of the dihedral angle. Such a conjugated structure became possible because of  $\pi$ -orbital bridging by the *d*-orbitals of the  $\text{Fe}^{3+}$  ion. The electron delocalization is maximized when the GQD-Fe-GQD assembly has a linear geometry. The requirement of the maximal delocalization for the GQD-Fe-GQD assembly translates into  $D_2$  symmetry of GQD-Fe-GQD unit as the elementary building block of the resulting self-assembled superstructure. Several computational and theoretical studies indicated that the symmetry of the building blocks propagate through the scales explicitly determining the geometry of the hierarchical assemblies formed via near-equilibrium processes,<sup>53–59</sup> which is the case for GQDs. Importantly, the characteristic  $C_2$  axis aligned with the planes of both graphene

sheets in the GQD-Fe-GQD unit is translated into axial bonding potential between them that, in some studies, is referred to as dipolar potential.<sup>55,57</sup> Combined with electrostatic repulsion limiting the radial growth from structural defects in GQDs, such bonding potential leads to linear assemblies preserving the  $C_2$  symmetry. On the other hand, variable dihedral angles between the graphene sheets in GQD-Al-GQD units destroys  $C_2$  operation placing structural units into the  $S_{2n}$  symmetry group. It concomitantly imparts large scale GQD-Al-GQD assemblies with a nearly isotropic bonding potential that translates into supraparticles formation when paired with the same electrostatic restrictions on their size.<sup>49</sup>

The electronic structure established from DFT calculations also helps us to explain the origin of Raman scattering enhancement. Similarly to previous studies of molecular systems of both organic and inorganic nature,<sup>60,61</sup> the increased delocalization of  $\pi$ -orbitals leads to the enhancement of Raman scattering, which can be directly inferred from the theory of Raman scattering for highly polarizable electronic systems.<sup>62</sup> The DFT-calculated Raman intensity showed a 16.5 times enhancement of the  $1600\text{ cm}^{-1}$  band attributed to the breath stretching vibration along the graphene layer after the formation of GQD-Fe<sup>3+</sup> nanochains, which corresponds well with the experimental results. Increased molecular rigidity is also responsible for an approximate 3.5 times enhancement of luminescence quantum yield, as illustrated in **Figure S3**.

***Molecular Dynamic Simulations:*** GQDs have smaller and lighter atoms than most metal, semiconductor, and ceramic NPs, which opens an opportunity to create a fully atomistic model for computational studies needed for assemblies driven by coordination bonds. Note that coarse grained models that would be suitable for the modeling of mesoscale structures would still require consideration of fully atomistic structures to establish bonding potentials and be bound

by the same symmetry rules. Also, important computational capabilities at the atomistic level are essential for modeling environmental processes consisting of a wide range of ionic components that is often impossible experimentally.

We constructed GQD-M-GQD and GQD-M-GQD-M-GQD models for assemblies bridged by  $\text{Fe}^{3+}$  and  $\text{Al}^{3+}$  that represent extended and terminal superstructures, respectively. Water molecules completed the coordination sphere of the metal centers containing six coordination bonds for  $\text{Fe}^{3+}$  and  $\text{Al}^{3+}$ . All MD experiments returned the equilibrated geometries of the GQD-M-GQD and GQD-M-GQD-M-GQD segments with a distinct linear configuration for  $\text{Fe}^{3+}$  (**Figure 4e, g**), whereas the same assemblies bridged by  $\text{Al}^{3+}$  equilibrated into the angled configuration. The difference in the shape of metal-GQD oligomers is attributed to the different coordination preferences of the metal ion determined by the lowest HOMO energy (**Figure 4c**), while other stimuli, such as attractive forces from coordination bonds (enumerated by  $K_c$ , which is  $\sim 1$  for both  $\text{Al}^{3+}$  and  $\text{Fe}^{3+}$ , **Figure 1g**) and electrostatic repulsion (enumerated by the overall charges of  $\text{M}^{n+}$  and GQDs), are comparable.  $\text{Fe}^{3+}$  ions strongly favor bidentate coordination of carboxyl groups but  $\text{Al}^{3+}$  prefers monodentate coordination according to our DFT calculations (**Figure S23**) and previous reports.<sup>63</sup> This geometry of the coordination bridges in the GQD-Fe-GQD assembly units forces them to align themselves with respect to each other, propagating the symmetry of the individual blocks through all the scales similarly to crystallographic relations in minerals, which can be recognized in their preferential formation of chains (**Supplementary Notes**). Thus, monodentate coordination ligands eliminate at least one symmetry relationship in the structural unit defining the preferential bonding axis, which leads to a supraparticle structure that maximizes short-range attractions. In agreement with this mechanism and DFT calculations above, the Raman spectra of GQD- $\text{Al}^{3+}$  supraparticles showed much lower (43%) Raman

scattering enhancement than GQD-Fe<sup>3+</sup> nanochains, reflecting more flexible assemblies (**Figure S25**). GQD-Al<sup>3+</sup> assemblies also revealed a much higher and broader  $G'_2$  band at 3000 cm<sup>-1</sup> than GQD-Fe<sup>3+</sup> due to stacking of graphene layers in the supraparticles.

**Comparison with nanoscale structure of shungite:** While there is wide variety of nanoscale colloids in the environment and an equally wide range of environmental conditions, self-assembled structures from nanocarbon particles observed for a well-known carbon-rich mineral, such as shungite<sup>64,65</sup> provides a convenient case for establishing the relationship between the nanoscale colloids and the resulting structure of minerals. This is because the identity of carbonaceous particles in the matrix of inorganic materials can be traced much better than that for ceramic NPs.

Multi-layer graphene nanosheets (**Figure 5a**), GQD-like dots, and their network assemblies (**Figure 5b,c**) were observed in the TEM images of the examined shungite samples. Interestingly, hollow nanoshells strikingly similar to those assembled from GQDs, also exist in shungite rocks (**Figure 5d**). XPS elemental analysis was employed to study the possible overlap in elemental composition between shungite samples and our as-prepared GQD assemblies. Our shungite contains approximately 70% carbon, 20% oxygen, 0.22% iron, and 1.42% aluminum (**Table S4**), which indicates that the examined rocks are fairly typical for this mineraloid that can display carbon content from 20% to 98%.

Raman spectra and synchrotron based small angle X-ray scattering (SAXS) spectra were carried out to provide detailed structural information of the carbonaceous assemblies in the rocks. The shungite showed a typical graphene-type Raman spectrum, with narrow and sharp  $D$  and  $G$  bands (**Figure 5e,f**). The synchrotron SAXS spectra provided structural information about

the ensemble properties of nanocarbon assemblies of the mineral. The SAXS spectrum for a water dispersion of milled shungite exhibited virtually identical scattering curves as those of the GQD assembled nanochains. From all the observations described, we believe that nanoparticles with high carbon content formed prior to the formation of this rock and were able to assemble into various architectures during its formation.

**CONCLUSIONS:** GQDs self-assemble via coordination bonds under ambient conditions into superstructures with unexpectedly wide morphological diversity. We elucidated the mechanism of GQD assembly and the emergence of specific patterns, such as nanochains and supraparticles formed by GQDs with  $\text{Fe}^{3+}$  and  $\text{Al}^{3+}$ , respectively, which replicate nearly exactly the nanoscale structures reported for shungite.<sup>66</sup> This observation opens a question how the conditions during the formation of this mineraloid might be related to the complex nanocarbon superstructures observed in it. The fact that shungite rocks are known to form as sediments in shallow lagoons<sup>67</sup> seems to be conducive with the organizational patterns of carbonaceous nanostructures in it. However, it is not clear how subsequent metamorphic processes might have affected the initial assemblies. The question about the origin of carbon-rich particles as the product of high-temperature decomposition of organic matter or the original components experienced self-assembly process might also be raised. For any genesis of the examined shungite rocks, the diversity of the observed superstructures and simplicity of their formation indicate the possibility of NP-based structures with life-like in geometry and functions.<sup>68,69</sup> The morphological complexity of these structures can mirror that observed for GQDs, albeit not being limited by it.

## **METHODS**

**Synthesis of graphene quantum dots (GQDs).** GQDs were synthesized by a modified protocol through a top-down “oxidation-cutting” process.<sup>45</sup> In detail, 50 mg of carbon fibers was dispersed into a 4 mL mixture of sulfuric acid and nitric acid (3:1 v/v). The black solution was subjected to sonication for 2 h and mechanically stirred for 24 h at 80 °C. After the reaction, the mixture was cooled and diluted with deionized (DI) water (0.15 mg/mL). Sodium hydroxide was added to adjust the solution to a neutral pH value. The mixture was dialyzed for 3 days to obtain the final product.

**Synthesis of GQD nanochains.** The GQD nanochains self-assembled after adding metal ions (e.g.  $\text{Fe}^{3+}$ ) to a dispersion of GQDs. Typically, HCl solution (0.1 mol/L) was added into 0.01 mg/mL solution of GQDs to keep the pH to around 3. After that,  $\text{FeCl}_3$  solutions were slowly mixed with the GQDs under mild shaking. The mixture was stored at room temperature overnight until the color of the solution darkened slightly. The product was purified using an ultrafiltration tube (molecular weight (M.W.) cutoff: 3000) spinning in a centrifuge (6000 rpm) for 0.5 h three times.

**Instrumentation.** The TEM characterization was performed using a JEOL 3011 HREM while a JEOL 2100F was employed for the HAADF and bright field (BF) imaging under STEM mode. STEM tomography was applied on a JEOL 2100F using a Gatan 912 tomographic holder under the control of a SerialEM program. An ETOMO program was used for tomographic reconstruction by means of a back-projection algorithm. AFM (Veeco, Dimension Icon AFM) and SEM (FEI, Nova 200 Nanolab SEM/FIB) were performed for the morphological studies of GQD- $\text{Fe}^{3+}$  nanochains. The elemental analysis was performed by XPS (Kratos, Axis Ultra XPS) and EDAX (EDAX XEDS system accessory to FEI Nova 200 Nanolab SEM/FIB). In order to confirm the accuracy and reliability of the data, the XPS in this experiment was calibrated using

a Au 4f 7/2 peak at 84.00 eV from gold film coating on a blank sample on a silicon wafer. Rigaku Ultima IV XRD was used for XRD and SAXS characterizations. The synchrotron based SAXS characterizations were carried out on a beamline BL19B1, Shanghai Synchrotron Radiation Facility.

The light emission properties of GQDs and their assemblies were investigated by fluorescence spectroscopy (Horiba, Fluoromax-3). The absorbance of the samples was analyzed by UV-Vis spectroscopy (Agilent, 89090A). The magnetic circular dichroism was analyzed by CD spectroscopy (JASCO, J-815) using a permanent magnet cuvette mount with 1 T of magnetic field intensity. The Raman spectra were measured by a Renishaw InVia Reflex Micro Raman Spectrometer while the FT-IR were obtained on a Nicolet 6700 FTIR spectrometer, which allowed for the study of the vibrational information of the molecules. The  $\zeta$ -potentials were measured by a Zetasizer (Malvern Instruments, Nano ZS). Confocal fluorescence microscopy (Leica, SP8 MP) was applied to monitor the formation of nanochains in situ.

## REFERENCES

1. Boles, M. A., Engel, M. & Talapin, D. V. Self-Assembly of Colloidal Nanocrystals: From Intricate Structures to Functional Materials. *Chem. Rev.* **116**, 11220–11289 (2016).
2. Kim, J.-Y. & Kotov, N. A. Charge transport dilemma of solution-processed nanomaterials. *Chem. Mater.* **26**, (2014).
3. Ariga, K. *et al.* Self-assembly as a key player for materials nanoarchitectonics. *Sci. Technol. Adv. Mater.* **20**, 51–95 (2019).
4. Kotov, N. A., Dékány, I. & Fendler, J. H. Ultrathin graphite oxide-polyelectrolyte composites prepared by self-assembly: Transition between conductive and non-conductive states. *Adv. Mater.* **8**, 637–641 (1996).
5. Zhang, N., Qiu, H., Si, Y., Wang, W. & Gao, J. Fabrication of highly porous biodegradable monoliths strengthened by graphene oxide and their adsorption of metal ions. *Carbon N. Y.* **49**, 827–837 (2011).

6. Kovalenko, M. V. *et al.* Prospects of Nanoscience with Nanocrystals. *ACS Nano* **9**, 150122081035000 (2015).
7. Hough, R. M. *et al.* Naturally occurring gold nanoparticles and nanoplates. *Geology* **36**, 571 (2008).
8. Tian, S., Wang, T., Li, G., Sheng, M. & Zhang, P. Nanoscale Surface Properties of Organic Matter and Clay Minerals in Shale. *Langmuir* **35**, 5711–5718 (2019).
9. Tepe, N. & Bau, M. Distribution of rare earth elements and other high field strength elements in glacial meltwaters and sediments from the western Greenland Ice Sheet: Evidence for different sources of particles and nanoparticles. *Chem. Geol.* **412**, 59–68 (2015).
10. Kumar, N., Shah, V. & Walker, V. K. Perturbation of an arctic soil microbial community by metal nanoparticles. *J. Hazard. Mater.* **190**, 816–22 (2011).
11. Karl, M., Leck, C., Coz, E. & Heintzenberg, J. Marine nanogels as a source of atmospheric nanoparticles in the high Arctic. *Geophys. Res. Lett.* **40**, 3738–3743 (2013).
12. Hawkings, J. R. *et al.* Biolabile ferrous iron bearing nanoparticles in glacial sediments. *Earth Planet. Sci. Lett.* **493**, 92–101 (2018).
13. Keith, D. W., Weisenstein, D. K., Dykema, J. A. & Keutsch, F. N. Stratospheric solar geoengineering without ozone loss. *Proc. Natl. Acad. Sci.* **113**, 14910 LP – 14914 (2016).
14. Tilmes, S. *et al.* Sensitivity of Aerosol Distribution and Climate Response to Stratospheric SO<sub>2</sub> Injection Locations. *J. Geophys. Res. Atmos.* **122**, 12,591–12,615 (2017).
15. Kotov, N. A. Self-assembly of inorganic nanoparticles: Ab ovo. *Europhys. Lett.* **119**, 66008 (2017).
16. Zhang, H. & Banfield, J. F. Nanoparticles in the Environment. *Rev. Mineral. Geochemistry* **44**, 1–58 (2001).
17. Reich, M. *et al.* Thermal behavior of metal nanoparticles in geologic materials. *Geology* **34**, 1033 (2006).
18. Ye, R. *et al.* Coal as an abundant source of graphene quantum dots. *Nat. Commun.* **4**, 2943 (2013).
19. Nowack, B. & Bucheli, T. D. Occurrence, behavior and effects of nanoparticles in the environment. *Environmental Pollution* **150**, 5–22 (2007).
20. Louie, S. M., Ma, R. & Lowry, G. V. Transformations of Nanomaterials in the Environment. *Front. Nanosci.* **7**, 55–87 (2014).
21. Wagner, S., Gondikas, A., Neubauer, E., Hofmann, T. & Von Der Kammer, F. Spot the difference: Engineered and natural nanoparticles in the environment-release, behavior, and fate. *Angewandte Chemie - International Edition* **53**, 12398–12419 (2014).
22. Penn, R. L. & Banfield, J. F. Imperfect Oriented Attachment: Dislocation Generation in Defect-Free Nanocrystals. *Science (80-. )*. **281**, 969–971 (1998).
23. Tang, Z., Kotov, N. A. & Giersig, M. Spontaneous organization of single CdTe nanoparticles into luminescent nanowires. *Science (80-. )*. **297**, 237–240 (2002).
24. De Yoreo, J. J. *et al.* Crystallization by particle attachment in synthetic, biogenic, and



- geologic environments. *Science* (80-. ). **349**, (2015).
25. Cölfen, H. & Antonietti, M. Mesocrystals: Inorganic superstructures made by highly parallel crystallization and controlled alignment. *Angewandte Chemie - International Edition* **44**, 5576–5591 (2005).
  26. Hirai, K. *et al.* Coordination Assembly of Discoid Nanoparticles. *Angew. Chemie Int. Ed.* **54**, 896 (2015).
  27. Pal, A., Bhakat, A. & Chattopadhyay, A. Zinc Ion-Induced Assembly of Crystalline Carbon Dots with Excellent Supercapacitor Performance. *J. Phys. Chem. C* **0**, null-null (2019).
  28. Hepel, M., Blake, D., McCabe, M., Stobiecka, M. & Coopersmith, K. *Assembly of Gold Nanoparticles Induced by Metal Ions*. ACS Symposium Series (American Chemical Society, 2012). doi:10.1021/bk-2012-1112.ch008
  29. Benselfelt, T., Nordenström, M., Hamed, M. M. & Wågberg, L. Ion-induced assemblies of highly anisotropic nanoparticles are governed by ion–ion correlation and specific ion effects. *Nanoscale* **11**, 3514–3520 (2019).
  30. Cong, H.-P., Ren, X.-C., Wang, P. & Yu, S.-H. Macroscopic Multifunctional Graphene-Based Hydrogels and Aerogels by a Metal Ion Induced Self-Assembly Process. *ACS Nano* **6**, 2693–2703 (2012).
  31. Canfield, D. E. Reactive iron in marine sediments. *Geochim. Cosmochim. Acta* **53**, 619–632 (1989).
  32. Morel, F. M. M., Milligan, A. J. & Saito, M. A. Marine Bioinorganic Chemistry: The Role of Trace Metals in the Oceanic Cycles of Major Nutrients. *Treatise on Geochemistry* 123–150 (2014). doi:10.1016/B978-0-08-095975-7.00605-7
  33. Homann, M. *et al.* Microbial life and biogeochemical cycling on land 3,220 million years ago. *Nat. Geosci.* **11**, 665–671 (2018).
  34. Dodd, M. S. *et al.* Evidence for early life in Earth’s oldest hydrothermal vent precipitates. *Nature* **543**, 60–64 (2017).
  35. Pan, D., Zhang, J., Li, Z. & Wu, M. Hydrothermal route for cutting graphene sheets into blue-luminescent graphene quantum dots. *Adv. Mater.* **22**, 734–738 (2010).
  36. Ponomarenko, L. A. *et al.* Chaotic Dirac Billiard in Graphene Quantum Dots. *Science* (80-. ). **320**, 356–358 (2008).
  37. Sun, H., Wu, L., Wei, W. & Qu, X. Recent advances in graphene quantum dots for sensing. *Mater. Today* **16**, 433–442 (2013).
  38. Yan, X., Cui, X. & Li, L.-S. Synthesis of large, stable colloidal graphene quantum dots with tunable size. *J. Am. Chem. Soc.* **132**, 5944–5 (2010).
  39. Li, K. *et al.* Technical synthesis and biomedical applications of graphene quantum dots. *J. Mater. Chem. B* **5**, 4811–4826 (2017).
  40. Shen, J., Zhu, Y., Yang, X. & Li, C. Graphene quantum dots: emergent nanolights for bioimaging, sensors, catalysis and photovoltaic devices. *Chem. Commun.* **48**, 3686 (2012).
  41. Zhang, X. *et al.* Direction-specific van der Waals attraction between rutile TiO<sub>2</sub>

- nanocrystals. *Science* (80-. ). **356**, 434 LP – 437 (2017).
42. Reich, M. *et al.* Thermal behavior of metal nanoparticles in geologic materials. *Geology* **34**, 1033 (2006).
  43. Ye, X. *et al.* Shape alloys of nanorods and nanospheres from self-assembly. *Nano Lett.* **13**, 4980–8 (2013).
  44. Bernatowicz, T. J. *et al.* Constraints on Stellar Grain Formation from Presolar Graphite in the Murchison Meteorite. *Astrophys. J.* **472**, 760–782 (1996).
  45. Peng, J. *et al.* Graphene quantum dots derived from carbon fibers. *Nano Lett.* **12**, 844–9 (2012).
  46. Qu, Z., Zhang, M., Zhou, T. & Shi, G. A Single-Wavelength-Emitting Ratiometric Probe Based on Phototriggered Fluorescence Switching of Graphene Quantum Dots. *Chem. - A Eur. J.* **20**, 13777–13782 (2014).
  47. Li, Q., Chen, B. & Xing, B. Aggregation Kinetics and Self-Assembly Mechanisms of Graphene Quantum Dots in Aqueous Solutions: Cooperative Effects of pH and Electrolytes. *Environ. Sci. Technol.* (2017). doi:10.1021/acs.est.6b04178
  48. The extended assemblies refer to non-random patterns that have no apparent limitations for at least one of the dimensions, whereas the terminal assemblies refer the motifs that display specific limitations for all the dimensions.
  49. Xia, Y. *et al.* Self-assembly of self-limiting monodisperse supraparticles from polydisperse nanoparticles. *Nat. Nanotechnol.* **6**, 580–7 (2011).
  50. Slotznick, S. P., Eiler, J. M. & Fischer, W. W. The effects of metamorphism on iron mineralogy and the iron speciation redox proxy. *Geochim. Cosmochim. Acta* **224**, 96–115 (2018).
  51. Williams, R. J. P. Iron in evolution. *FEBS Lett.* **586**, 479–484 (2012).
  52. Ferrari, A. C. & Basko, D. M. Raman spectroscopy as a versatile tool for studying the properties of graphene. *Nat. Nanotechnol.* **8**, 235–246 (2013).
  53. Guo, J. *et al.* Modular assembly of superstructures from polyphenol-functionalized building blocks. *Nat. Nanotechnol.* 1–8 (2016). doi:10.1038/nnano.2016.172
  54. Morphey, D., Shaw, J., Avins, C. & Chakrabarti, D. Programming Hierarchical Self-Assembly of Patchy Particles into Colloidal Crystals via Colloidal Molecules. *ACS Nano* **12**, 2355–2364 (2018).
  55. Van Workum, K. & Douglas, J. Symmetry, equivalence, and molecular self-assembly. *Phys. Rev. E* **73**, 031502 (2006).
  56. Grünwald, M. & Geissler, P. L. Patterns without patches: hierarchical self-assembly of complex structures from simple building blocks. *ACS Nano* **8**, 5891–5897 (2014).
  57. Gröschel, A. H. *et al.* Guided hierarchical co-assembly of soft patchy nanoparticles. *Nature* **503**, 247 (2013).
  58. Liljeström, V., Mikkilä, J. & Kostianen, M. A. Self-assembly and modular functionalization of three-dimensional crystals from oppositely charged proteins. *Nat. Commun.* **5**, 4445 (2014).

59. Qiu, H., Hudson, Z. M., Winnik, M. A. & Manners, I. Multidimensional hierarchical self-assembly of amphiphilic cylindrical block comicelles. *Science (80-. )*. **347**, 1329 LP – 1332 (2015).
60. Castiglioni, C., Del Zoppo, M. & Zerbi, G. Vibrational Raman spectroscopy of polyconjugated organic oligomers and polymers. *J. Raman Spectrosc.* **24**, 485–494 (1993).
61. Agosti, E., Rivola, M., Hernandez, V., Del Zoppo, M. & Zerbi, G. Electronic and dynamical effects from the unusual features of the Raman spectra of oligo and polythiophenes. *Synth. Met.* **100**, 101–112 (1999).
62. Masiello, D. J. & Schatz, G. C. Many-body theory of surface-enhanced Raman scattering. *Phys. Rev. A* **78**, 42505 (2008).
63. Bala, T., Prasad, B. L. V., Sastry, M., Kahaly, M. U. & Waghmare, U. V. Interaction of Different Metal Ions with Carboxylic Acid Group: A Quantitative Study. *J. Phys. Chem. A* **111**, 6183–6190 (2007).
64. Razbirin, B. S., Rozhkova, N. N., Sheka, E. F., Nelson, D. K. & Starukhin, a N. Fractals of graphene quantum dots in photoluminescence of shungite. *J. Exp. Theor. Phys.* **118**, 735–746 (2014).
65. Razbirin, B., Rozhkova, N. & Sheka, E. Spectral properties of shungite quantum dots. *Nanosyst. Physics, Chem. Math.* **5**, 217–233 (2014).
66. Kovalevski, V. V., Buseck, P. R. & Cowley, J. M. Comparison of carbon in shungite rocks to other natural carbons: An X-ray and TEM study. *Carbon N. Y.* **39**, 243–256 (2001).
67. Melezhik, V. A., Filippov, M. M. & Romashkin, A. E. A giant Palaeoproterozoic deposit of shungite in NW Russia: genesis and practical applications. *Ore Geol. Rev.* **24**, 135–154 (2004).
68. Yang, M. *et al.* Self-assembly of nanoparticles into biomimetic capsid-like nanoshells. *Nat Chem* **9**, 287–294 (2017).
69. Li, Z. *et al.* An embryo of protocells: The capsule of graphene with selective ion channels. *Sci. Rep.* **5**, 10258 (2015).

**ACKNOWLEDGEMENTS:** The central part of this work was supported by the NSF 1463474 project “*Energy- and Cost-Efficient Manufacturing Employing Nanoparticles*”. The authors also thank the Chinese Scholarship Council (CSC) for the research scholarship to Z.B.Q. Partial support of this work was also provided by NSF 1566460 *Nanospiked Particles for Photocatalysis*; NSF 1538180 *Layered Composites from Branched Nanofibers for Lithium Ion Batteries*; **MURI:** Department of-Army W911NF-10-1-0518 *Reconfigurable Matter from*

*Programmable Colloids*; AFOSR FA9550-16-1-0265, *Nanocomposite Ion Conductors for Thin Film Batteries*. All of the authors thank the Michigan Center for Materials Characterization (MC<sup>2</sup>) for its assistance with electron microscopy. NSF grant #DMR-9871177 is gratefully acknowledged for funding of the JEOL 2010F analytical electron microscope used in this work.

**AUTHOR CONTRIBUTIONS:** Z.B.Q. and W.F. designed some and performed the experiments. Z.B.Q. and Y.W. designed and conducted the computational simulations. Z.B.Q. and N.A.K. wrote the paper. All the authors contributed to the writing and editing of individual sections of the manuscript. N.A.K. conceived the project and designed some of the experiments.

**ADDITIONAL INFORMATION:** Supplementary information is available in the online version of the paper. Reprints and permissions information is available online at [www.nature.com/reprints](http://www.nature.com/reprints). Correspondence and requests for materials should be addressed to N.A.K.

**COMPETING FINANCIAL INTERESTS:** The authors declare no competing financial interests.

Author Manuscript

## FIGURES:

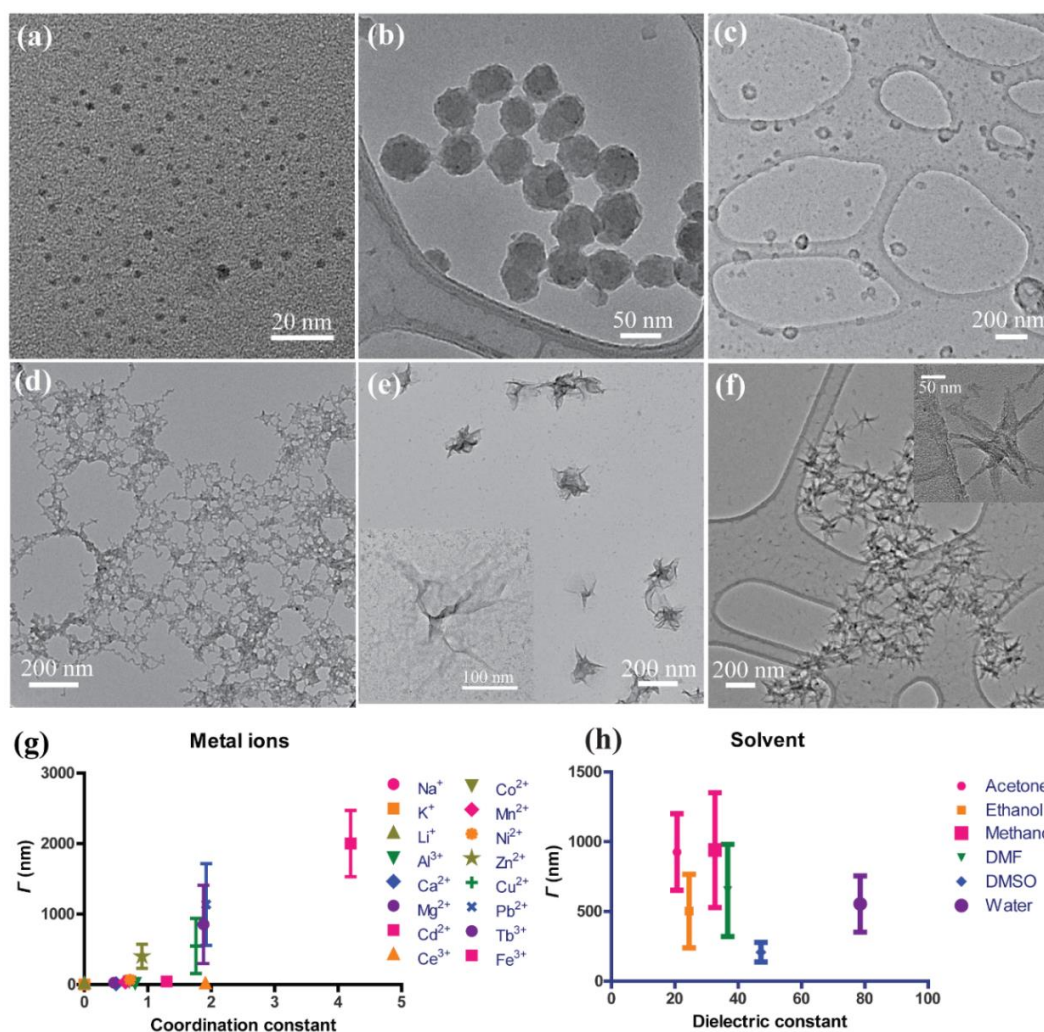


**Figure 1 | Coordination assemblies of GQDs with various morphologies.** (a-d) TEM images of equilibrium GQD assemblies induced by 0.5 mM of (a) Na<sup>+</sup>, (b) Al<sup>3+</sup>, (c) Ni<sup>2+</sup>, and (d) Fe<sup>3+</sup> after 24 h assembly process for [GQD] = 0.01 mg/mL, pH 3.0 in water. (e-f) TEM images GQD coordination assemblies induced by (e) 0.5 mM Fe<sup>3+</sup> for [GQD] = 0.1 mg/mL, pH 3.2 in ethanol/water 4:1 solution and (f) 1 mM Fe<sup>3+</sup> for [GQD] = 0.01 mg/mL, pH 3.5 in water. (g-h) The dependence of the largest geometrical measure,  $\Gamma$ , of the coordination assemblies on (g) the coordination constant for carboxyl group with the metal ion and (h) dielectric constant of the

media. Hausdorff geometry of sets utilizes  $\Gamma$  to describe complex objects with multiple characteristics that GQD assemblies represent. Within the framework of this study, larger  $\Gamma$  represents a greater propensity of the system toward self-assembly with a pattern characteristic for specific GQD- $M^{n+}$  systems.  $\Gamma$  for GQD- $M^{n+}$  assemblies were calculated depending on the geometry of the spontaneously forming constructs as the average total length for chains, average largest XY dimension for sheets, and average diameter for supraparticles, nanoshells, or stars.

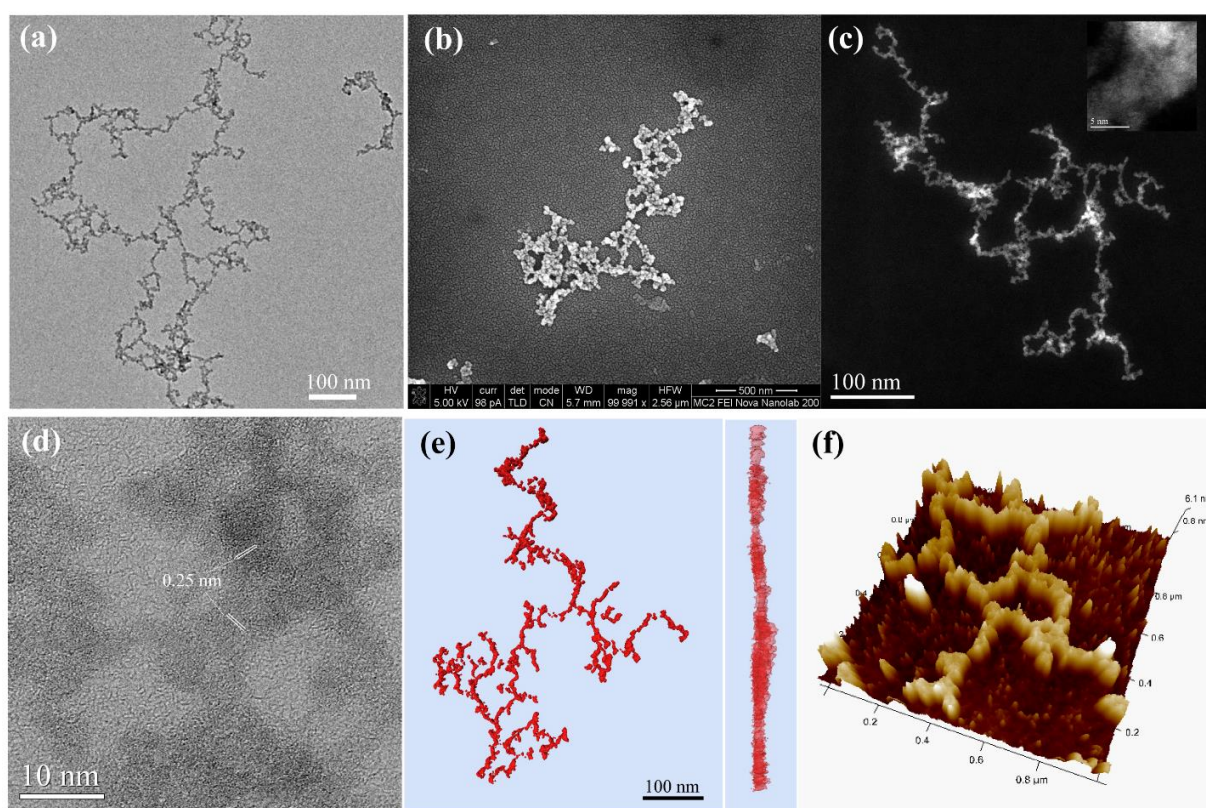


**Figure 2 | Structural characterizations of GQD- $Fe^{3+}$  nanochains.** TEM image (a), SEM image (b), HAADF-STEM image (c), high resolution BF-STEM image, reconstructed 3D tomographic model in top view (e left) and side view (e right), and AFM height topological image (f) of GQD- $Fe^{3+}$  nanochains. Inset: high resolution HAADF-STEM image for a selective

part of the GQD-Fe<sup>3+</sup> nanochain. The GQD-Fe<sup>3+</sup> nanochains were assembled at 10 μg/mL GQD and 0.5 mM Fe<sup>3+</sup> ions under pH 3.2.

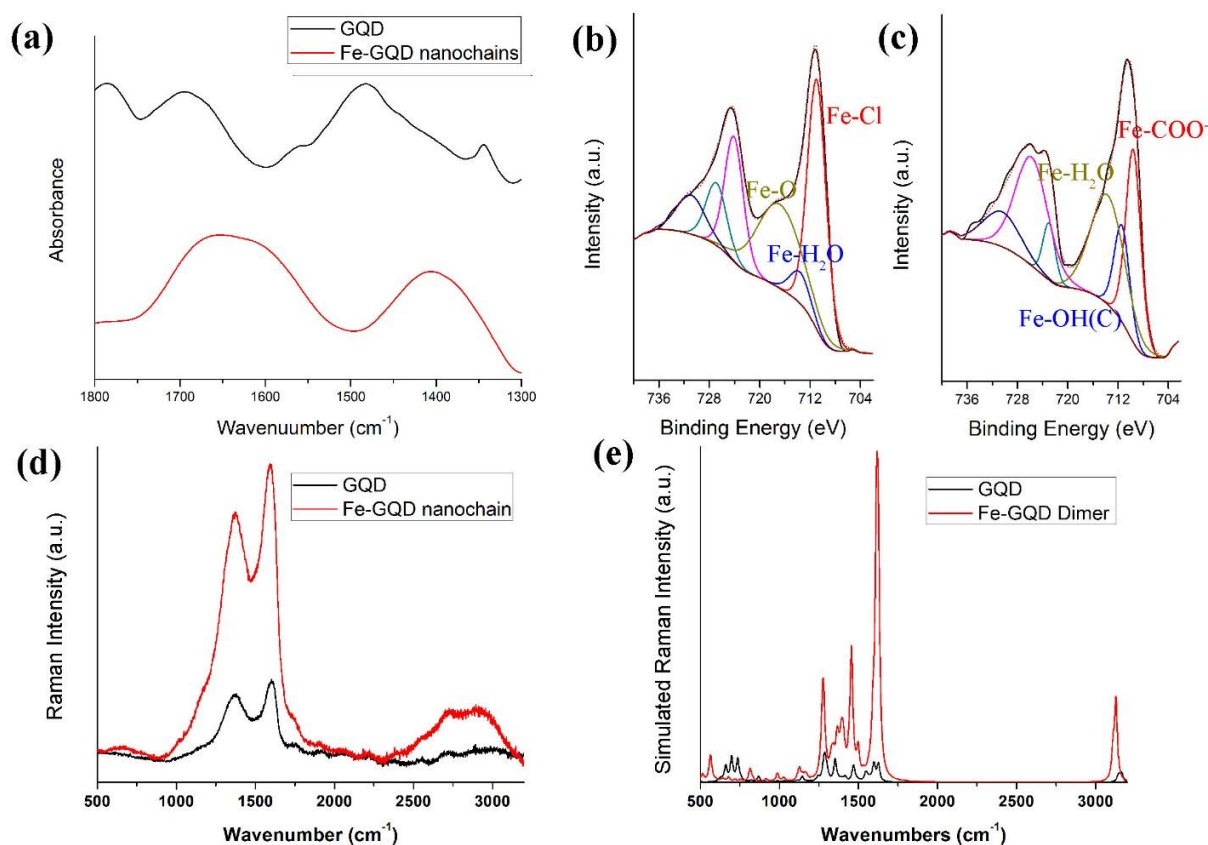


**Figure 3 | Spectroscopic characterizations of GQD-Fe<sup>3+</sup> nanochains.** (a) FT-IR spectra for GQD and GQD-Fe<sup>3+</sup> nanochains. High resolution XPS of Fe 2p for dried Fe<sup>3+</sup> solution (b) and GQD-Fe<sup>3+</sup> nanochains (c). Experimental Raman spectra (d) for GQDs and GQD-Fe<sup>3+</sup> nanochains. Simulated Raman spectra (e) for GQD and GQD-Fe<sup>3+</sup> dimers calculated using density functional theory (DFT). The GQD-Fe<sup>3+</sup> nanochains were assembled at 10 μg/mL GQD and 0.5 mM Fe<sup>3+</sup> ions under pH 3.2.

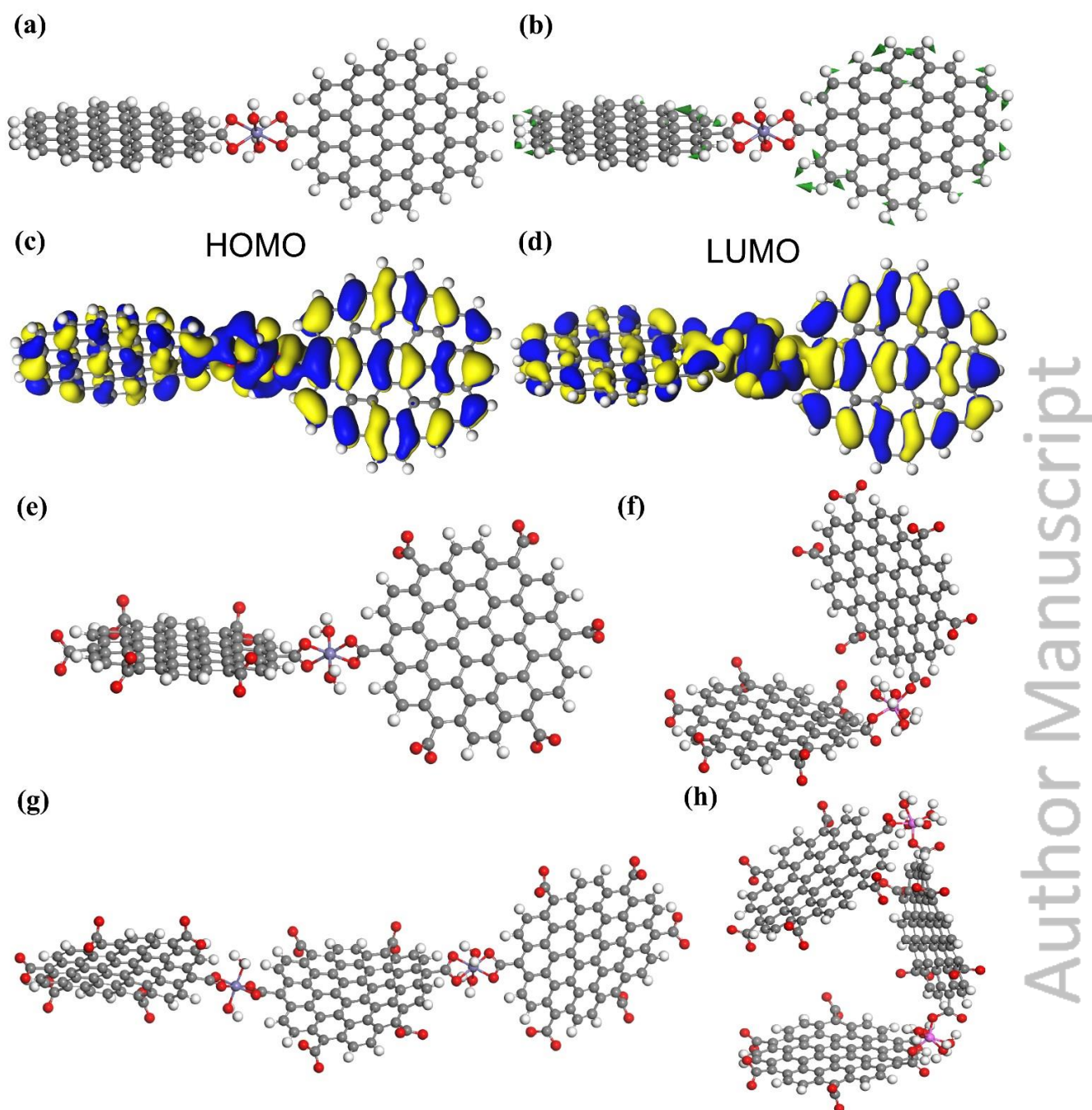


**Figure 4 | Computational studies of coordination assemblies of GQDs.** (a) Optimized molecular geometry for GQD-Fe<sup>3+</sup> dimer obtained by DFT. (b) Vibration mode for GQD-Fe<sup>3+</sup> dimer at 1611 cm<sup>-1</sup> through DFT-based vibrational analysis. Molecular orbitals for bidentate GQD-GQD-Fe<sup>3+</sup> assemblies: (c) HOMO and (d) LUMO. The isovalue for the orbital mapping



was set to 0.15 eV. (e-h) Optimized geometries obtained by MD simulations for (e) GQD-Fe<sup>3+</sup> dimer, (f) GQD-Al<sup>3+</sup> dimer, (g) GQD-Fe<sup>3+</sup> trimer, and (h) GQD-Al<sup>3+</sup> trimer. Color coding: gray - carbon, red - oxygen; white - hydrogen; blue - iron; pink - aluminum. Blue solid - positive orbital; yellow solid -negative orbital.

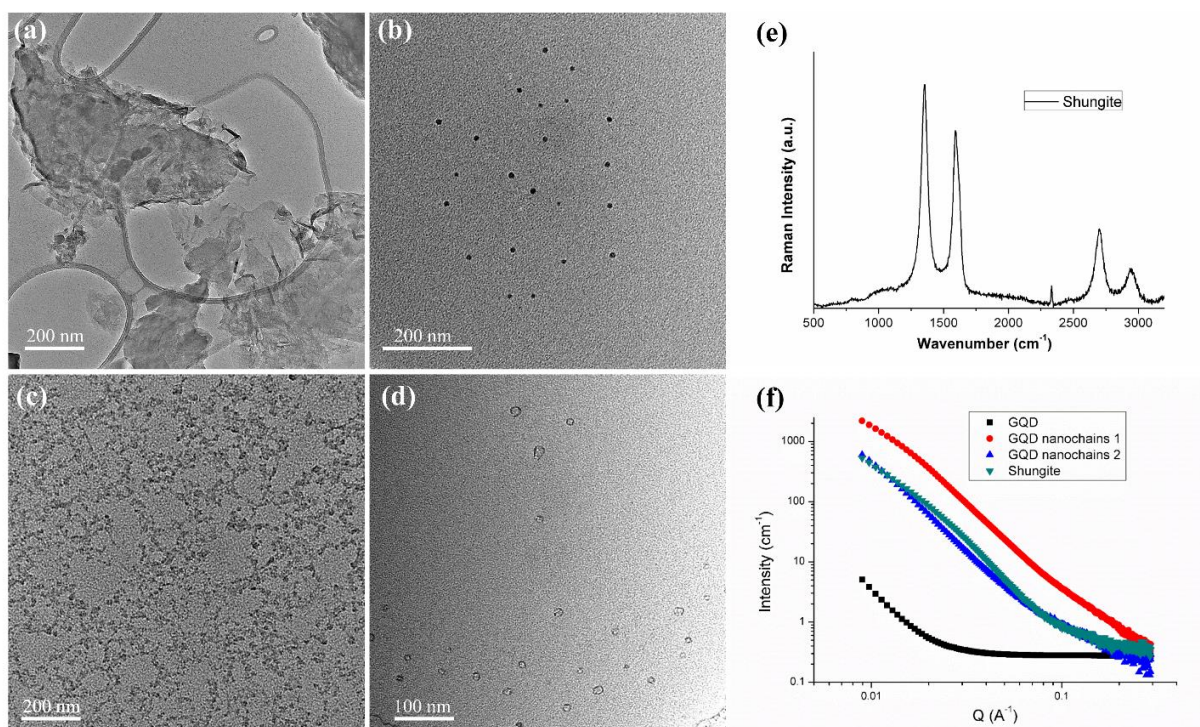


**Figure 5 | Experimental data on nanostructures in shungite.** TEM images of (a) graphite fractals and graphene layers, (b) carbon nanodots, (c) nanochain networks, and (d) nanoshells in shungite samples. (e) Raman spectra for shungite rocks. (f) Synchrotron based SAXS spectra for Fe-GQD nanochains. The GQD nanochains 1 were fabricated at [Fe<sup>3+</sup>] = 2 mM, [GQD] = 10 µg/mL, and pH 3.2. The GQD nanochains 2 were fabricated at [Fe<sup>3+</sup>] = 0.5 mM, [GQD] = 10 µg/mL, and pH 3.2. And the GQD and shungite solutions were both 10 µg/mL at pH 3.2, adjusted by HCl.